Available online at www.sciencedirect.com
SCIENCE DIRECT®
ELSEVIER
Earth and Planetary Science Letters 215 (2003) 219–235
EPSL
www.elsevier.com/locate/epsl

Comparison of smectite- and illite-rich gouge frictional properties: application to the updip limit of the seismogenic zone along subduction megathrusts

Demian M. Saffer [a,*], Chris Marone [b]

[a] Department of Geology and Geophysics, University of Wyoming, Laramie, WY 82071-3006, USA
[b] Department of Geosciences, Pennsylvania State University, University Park, PA 16802, USA

Received 8 May 2003; received in revised form 18 July 2003; accepted 22 July 2003

Abstract

Along plate boundary subduction thrusts, the transformation of smectite to illite within fault gouge at temperatures of ~150°C is one of the key mineralogical changes thought to control the updip limit of seismicity. If correct, this hypothesis requires illite-rich gouges to exhibit frictionally unstable (velocity-weakening) behavior. Here, we report on laboratory experiments designed to investigate the frictional behavior of natural and synthetic clay-rich gouges. We sheared 5-mm-thick layers of commercially obtained pure Ca-smectite, a suite of smectite–quartz mixtures, and natural illite shale (grain size ranging from 2 to 500 μm) in the double-direct shear geometry to shear strains of ~7–30 at room humidity and temperature. XRD analyses show that the illite shale contains dominantly clay minerals and quartz; within the clay-sized fraction (< 2 μm), the dominant mineral is illite. Thus, we consider this shale as an appropriate analog for fine-grained sediments incoming to subduction zones, within which smectite has been transformed to illite. We observe a coefficient of friction (μ) of 0.42–0.68 for the illite shale, consistent with previous work. Over a range of normal stresses from 5 to 150 MPa and sliding velocities from 0.1 to 200 μm/s, this material exhibits only velocity-strengthening behavior, opposite to the widely expected, potentially unstable velocity-weakening behavior of illite. Smectite sheared under identical conditions exhibits low friction ($\mu = 0.15$–0.32) and a transition from velocity weakening at low normal stress to velocity strengthening at higher normal stress (> 40 MPa). Our data, specifically the velocity-strengthening behavior of illite shale under a wide range of conditions, do not support the hypothesis that the smectite–illite transition is responsible for the seismic–aseismic transition in subduction zones. We suggest that other depth- and temperature-dependent processes, such as cementation, consolidation, and slip localization with increased shearing, may play an important role in changing the frictional properties of subduction zone faults, and that these processes, in addition to clay mineralogy, should be the focus of future investigation.

Keywords: subduction zones; fault mechanics; seismogenic zone; smectite illite; laboratory experiments

1. Introduction

The world's largest and most destructive earthquakes occur along subduction zone thrusts. Sub-

* Corresponding author. Tel.: +1-307-766-2981.
E-mail address: dsaffer@uwyo.edu (D.M. Saffer).

0012-821X/03/$ – see front matter © 2003 Elsevier B.V. All rights reserved.
doi:10.1016/S0012-821X(03)00424-2

duction plate boundaries are seismic over a limited depth range; slip is dominantly aseismic at depths shallower than a few kilometers and deeper than ~40–50 km (e.g., [1–3]). Thus, subduction plate boundaries are divided into three main zones: an aseismic 'updip' zone, the seismogenic zone, and a deep 'downdip' aseismic zone (e.g., [1]) (Fig. 1). Defining the locations and controlling mechanisms of both the updip and downdip limits of the seismogenic zone remain crucial steps toward defining the width of the seismogenic zone and the maximum magnitude of potential earthquakes. The updip limit of the seismogenic zone is of particular importance in tsunami generation, whereas the downdip limit determines the landward extent of earthquake generation along the interface.

Hypothesized mechanisms explaining the downdip limit of interplate seismicity include (1) the onset of crystal plasticity and associated creep behavior at ~350–450°C, with the exact temperature depending upon mineralogy (e.g., [1,4–6]), and (2) the intersection of the subducting slab with the forearc mantle wedge in colder subduction zones (e.g., [6]). There has been comparatively little work focused on processes that control the updip limit of seismogenic faulting (e.g., [7,8]).

In the context of evaluating hypothesized controls on the seismogenic zone, one approach is to employ laboratory-based friction laws coupled with stability analysis to account for continuum interactions. Frictional velocity dependence is considered the most likely explanation for differences between stable sliding (aseismic) and unstable stick-slip (seismogenic) behavior (e.g., [9,10]). Materials that exhibit velocity strengthening (frictional resistance increases with sliding velocity) produce only inherently stable frictional slip, whereas those that exhibit velocity-weakening frictional behavior may exhibit either unstable stick-slip or conditionally stable behavior. Increasing effective stress leads to a greater tendency for unstable sliding in velocity-weakening materials, as noted by Scholz [10], who defined a stability parameter: $\xi=(a-b)\cdot\sigma'_n$, where $(a-b)$ is the velocity dependence of sliding friction (negative values reflect velocity weakening) and σ_n' is effective stress. As the stability parameter ζ becomes more negative, the tendency for unstable slip increases.

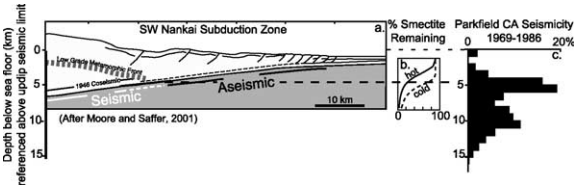

Fig. 1. (a) Schematic cross section of the SW Nankai subduction zone, showing extent of the 1946 coseismic rupture and inferred low-grade metamorphic front (after Moore and Saffer [7]). (b) Estimated progress of the smectite–illite transformation along the SW Nankai subduction megathrust, modeled using the kinetic expression of Pytte and Reynolds [11]. The two curves correspond to heat flow values of 150 mW/m^2 (cold) and 180 mW/m^2 (hot). (c) Distribution of seismicity at Parkfield from 1969 to 1986 as a function of depth (after Marone and Scholz [8]). The thin dashed line indicates zero depth for the two areas, registered to the seafloor above the updip extent of 1946 rupture at Nankai, and to the land surface at Parkfield. The heavy dashed line denotes the approximate depth of the updip limit for the 1946 rupture at Nankai; note that it corresponds with both the depth of significant smectite transformation (panel b) and the upper limit of seismicity at Parkfield (panel c).

One leading hypothesis for explaining the onset of seismogenic behavior in subduction zones is that the transformation of smectite to illite within fault gouge drives a transition from stable to unstable slip. The popularity of this hypothesis is due to (1) studies indicating that the thermally driven dehydration of smectite to illite is completed by temperatures of 120–150°C (e.g., [11]), (2) laboratory studies that demonstrate a difference in frictional strength between smectite- and illite-rich gouges, and (3) correlation between the location of the 150°C isotherm along subduction faults predicted by thermal models, and the observed seismic front along the Nankai, Cascadia, South Alaska, and Chile subduction zones [1,12].

Despite the fact that clay minerals are abundant in fault gouges (e.g., [13]), few detailed experiments have measured frictional properties of realistic analogs for natural fault gouges, which are typically composed of clays and quartz, with smaller amounts of other minerals including plagioclase, chlorite, and calcite (e.g., [13]). Existing work has generally focused on measurements of bulk frictional strength (e.g., [14–16]), and on the

observation of either stick-slip or stable sliding behavior in clay-rich gouges (e.g., [17]); detailed characterization of constitutive parameters over a wide range of experimental conditions (e.g., normal stress, sliding velocity, shear strain, temperature) has been lacking.

Existing studies have shown conclusively that smectite (hydrous) clays are frictionally weak (coefficient of friction $\mu = \sim 0.1$–0.3) and generally velocity strengthening (e.g., [15,18–20]). Experimental data also show that illite (non-swelling) clays are frictionally stronger than smectite ($\mu = \sim 0.35$–0.49) (e.g., [14–16,21]). Although the transformation from smectite to illite is accompanied by an increase in frictional strength, few observations exist to test the hypothesis that the clay transformation results in a shift to frictionally unstable (velocity-weakening) behavior. A limited body of work has shown that illite-rich gouge exhibits stick-slip behavior at shear strains < 5 and temperatures of 400–600°C, and that this behavior may be related to fabric development [17].

Here, we report on a series of direct shear experiments conducted on commercially obtained smectite powder, smectite–quartz mixtures, and natural illite shale, which serve as reasonable analogs for natural fault gouges of mixed composition (e.g., [13]). These experiments are designed to test the hypothesis that illite-rich gouge is velocity weakening – and therefore that the transformation from smectite to illite controls the updip limit of subduction zone seismicity.

2. Methods

We sheared layers of Ca-smectite powder, smectite–quartz mixtures ranging from 0% to 100% smectite, and granulated illite-rich shale (Rochester Shale) with grain sizes ranging from 2 to 500 μm in the double-direct shear geometry (Fig. 2), to shear strains of 7–30 at room humidity and temperature. We obtained smectite as a powder (GSA resources, SM1502A) and the illite shale as rock fragments (Ward's Geological Supply), which we then crushed, powdered in a rotary mill, and sieved to < 500 μm grain size. We conducted detailed X-ray diffraction (XRD) analyses

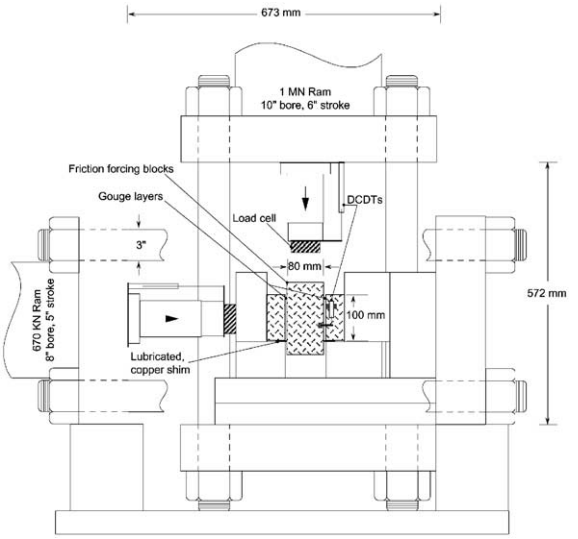

Fig. 2. Schematic of biaxial shear device indicating sample geometry and load frame configuration. Each load frame is independently controlled by a high-speed servo-hydraulic system. For these experiments, normal stress was applied as a constant force boundary condition and shear stress was applied as a constant shear displacement rate.

on bulk powders and on oriented glycolated subsamples of the clay-sized (< 2 μm) fraction.

XRD analyses confirm that the Ca-smectite powder is dominantly smectite, with small amounts of zeolite (clinoptilolite/heulandite), feldspar, and unaltered volcanic glass. The smectite contained $\sim 11\%$ water by weight prior to shearing, consistent with either fully hydrated single water interlayers (Bird's [22] hydration phase Ih), or partially hydrated smectite with two water interlayers (Bird's [22] hydration phase II-6). XRD analyses indicate that the illite shale is primarily composed of clay minerals (68%), quartz (23%), and plagioclase (4%) (Fig. 3a). Of the clay-sized fraction, 87% is illite and 13% is kaolinite/dickite (Fig. 3b), and the illite crystallinity is consistent with advanced diagenesis.

The compositions of illite shale and smectite–quartz mixtures used in our experiments are comparable to those of clay-rich fault gouges (e.g., [13,23–27]), materials used in previous experimental work (e.g., [17]), and the marine sediments that serve as source material for fault gouge in subduction zones (e.g., [23–26]). For example, sedi-

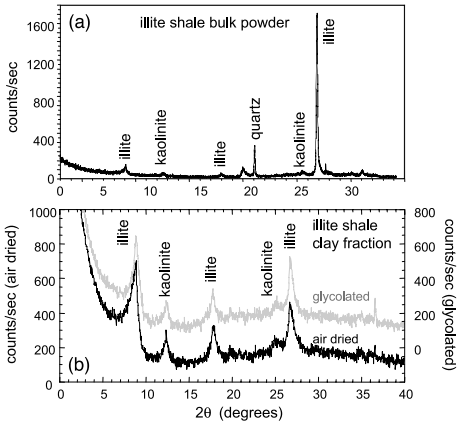

Fig. 3. X-ray diffractograms for (a) illite shale bulk powder and (b) illite shale clay-sized fraction (< 2 μm), with peaks annotated to denote mineralogy. For the clay separate, the black line shows data for the air-dried sample, and the gray line shows glycolated data for the same sample. Glycolated and air-dried traces are plotted on different axes for comparison of peaks. Peaks that shift after glycolation reflect the presence of swelling clay minerals (smectite in this case). Note that the sample contains little swelling clay, and that the dominant clay mineral is illite.

ments incoming to the SW Nankai subduction zone recovered by drilling on Ocean Drilling Program (ODP) Leg 190, sampled at the décollement, contain ~37–58% clay minerals, 30–42% quartz, 7–13% plagioclase, and 0–11% calcite. Of the clay minerals, 74–83% is illite–smectite; the remainder is dominantly chlorite [23].

Using unsaturated samples allowed us to characterize the mechanical properties of the gouges, while minimizing the effect of transient pore pressure changes in low-permeability clays. However, it is important to note that adsorbed water has been shown to decrease the frictional strength of some clays, including smectite (e.g., [16]). Previous work has shown that saturation has little influence on the strength of illite-rich gouge [14,15], consistent with the fact that illite is not a hydrous clay mineral. These observations suggest that saturation state may not affect illite frictional properties significantly, although additional experiments are clearly needed. Ultimately, the frictional characteristics of the gouge material and direct measurements of dilation in laboratory experiments (as discussed in Section 4.3) should be integrated with rupture models that treat transient pore water pressurization and volume change explicitly (e.g., [28]).

We constructed gouge layers by smoothing the powder onto grooved steel forcing blocks in a leveling jig. The initial thickness, (precisely 5 mm prior to the application of normal load for smectite, 7 mm for illite shale), was identical in each experiment for each gouge material. Initial compaction of the gouge upon application of normal stress decreased layer thickness to ~2–3 mm in all cases (Table 1). Layers were not subject to tamping or vibrations before being placed into the apparatus. A precise measurement of layer thickness, ±0.1 mm, was made in the apparatus under applied normal load at the start of each experiment, and changes in thickness were measured continuously to ±0.1μm throughout shearing. We report our results using average shear strain, calculated as the integral of displacement divided by instantaneous layer thickness.

We investigated the frictional strength and velocity dependence of sliding friction over a range of normal stresses from 5 to 150 MPa and sliding velocities from 0.1 to 200 μm/s. In each experiment, we recorded shear and normal stresses and displacements. The resolution of stress and displacement measurements is < 0.01 MPa and 0.1 μm, respectively. We calculate and report values of sliding friction coefficient as $\mu = \tau/\sigma_n$ (as shown in Figs. 4 and 5) where τ is shear stress at steady state and σ_n is normal stress.

We conducted multiple velocity steps in each experiment, over a wide range of shear strain (~3–25) after steady-state sliding was achieved (typically shear strains of 2–3) (Fig. 4). Step changes in sliding velocity result in a sharp change in friction coefficient, termed the direct effect (Figs. 4 and 6). The direct effect, a, is always of the same sign as the velocity change. With continued displacement, the coefficient of friction decays to a steady-state value for the new sliding velocity. The magnitude of this decay, b, is termed the evolution effect. We report the velocity dependence of sliding friction as $(a-b) = \Delta\mu/\Delta\ln V$, where V is sliding velocity. Negative values of $(a-b)$ reflect velocity-weakening behavior. Positive values of $(a-b)$ reflect velocity strengthening,

which results in stable sliding (e.g., [9]). We define the upstep velocity as the higher of the two sliding velocities in each velocity-step experiment.

3. Results

3.1. Frictional strength

For smectite and smectite–quartz mixtures, our strength data indicate a distinct peak and subsequent decay in shear strength during the first 5 mm of shear (shear strains from 0 to ~3) (Fig. 4) [20]. In general, steady-state sliding friction was reached after shear strains of ~2–3. The initial stress–strain behavior varied strongly with normal stress and quartz content. For a given composition, the magnitude of the initial peak stress increased with increased normal stress, whereas the strain necessary to reach steady sliding friction decreased [20]. The magnitude of the peak stress decreased with increased quartz content, and the strain needed to reach steady sliding friction increased (Fig. 4).

Illite shale also exhibits a distinct peak in strength at shear strains of ~1–3, followed by a decrease to steady-state sliding friction. This peak is comparable to that observed in smectite–quartz mixtures with ≥50% quartz, and the decay to steady-state friction occurred at similar shear strains (Fig. 4a,b). Illite shale has nearly the same shear strength and failure envelope as smectite–quartz mixtures with ≥70% quartz (Figs. 4 and 5).

Table 1
List of names, gouge material used, normal stresses, sliding velocities, and initial thicknesses (under normal load in the biaxial rig) for each experiment

Experiment	Gouge	σ_n (MPa)	Sliding velocities (μm/s)	Thickness (μm)
m333S3mr025	10% Smectite–90% Quartz	25	1, 10, 100	2100
m336S3mr025	50% Smectite–50% Quartz	25	1, 2, 10, 20, 100, 200	2275
m337S3mr025	90% Smectite–10% Quartz	25	1, 2, 10, 20, 100, 200	2100
m338S3mr025	70% Smectite–30% Quartz	25	1, 2, 10, 20, 100, 200	2100
m339S3mr025	30% Smectite–70% Quartz	25	1, 2, 10, 20, 100, 200	2100
m398S3mr020	Smectite	20	1, 10, 100	2250
m413S3mr005	Smectite	5	1, 10, 100	2800
m414S3mr010	Smectite	10	1, 10, 100	2480
m415S3mr015	Smectite	15	1, 10, 100	2350
m417S3mr025	Smectite	25	1, 10, 100	2150
m418S3mr030	Smectite	30	1, 10, 100	2050
m419S3mr035	Smectite	35	1, 10, 100	1960
m420S3mr040	Smectite	40	1, 10, 100	1875
m421S3mr045	Smectite	45	1, 10, 100	1850
m422S3mr050	Smectite	50	1, 10, 100	1825
m447S3mr015	Smectite	15	1, 10, 100	2250
m448S3mr015	Smectite	15	1, 10, 100	2330
m503S7ir040	Illite shale	40	2, 20, 200	2975
m504S7ir005	Illite shale	5	2, 20, 200	3275
m505S7ir020	Illite shale	20	2, 20, 200	2750
m506S7ir010	Illite shale	10, 20, 30	2, 20, 200	2738
m507S7ir050	Illite shale	25, 50	2, 20, 200	2575
m513S7ir010	Illite shale	10	1, 10, 100	2700
m514S7ir050	Illite shale	50, 75, 100, 150	2, 20, 200	2725
p034s7ir080	Illite shale	80, 120	2, 20, 200	1500
p035s7mr080	Smectite	75, 110	2, 20, 200	2000
p036s7mr050	Smectite	50, 100, 150	2, 20, 200	2200
p039s5mr060	50% Smectite–50% Quartz	60, 80, 120, 145	2, 20, 200	1750
p040s7mr060	Smectite	60, 80, 130, 145	2, 20, 200	1900

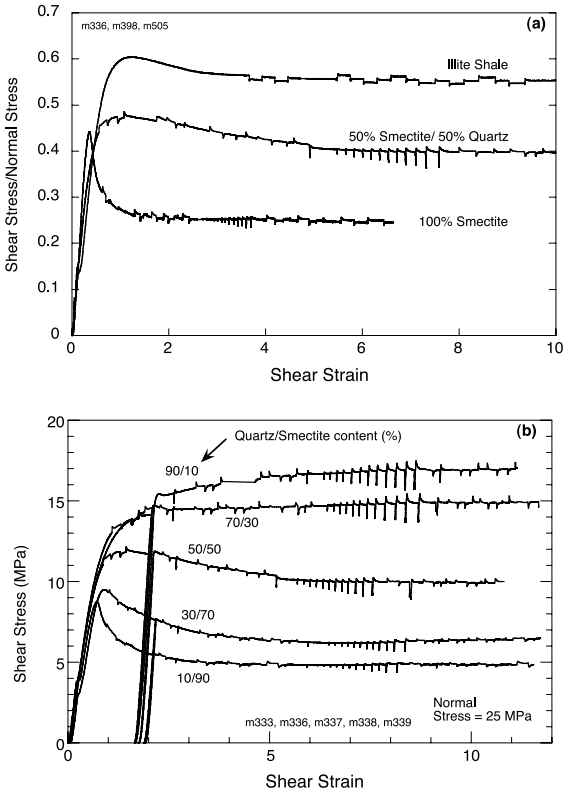

Fig. 4. Frictional strength vs. shear strain showing data for (a) illite shale, smectite, and a 50% mixture of quartz powder and smectite by weight, at 20 MPa normal stress, and (b) smectite–quartz mixtures ranging from 10% to 90% quartz, at 25 MPa normal stress. Experiment numbers used to generate the plots are listed (see Table 1).

For 100% smectite, the coefficient of sliding friction (μ) ranged from 0.07 to 0.30, and decreased with increasing normal stress (Fig. 5). For smectite–quartz mixtures, μ ranged from $\sim$0.2 to 0.53, increasing with quartz content and decreasing with normal stress. For illite shale, the coefficient of sliding friction ranged from 0.41 to 0.63 (Fig. 5a,b). The experimentally determined failure envelope for smectite changes slope at an effective normal stress of 30–40 MPa (Fig. 5a), indicating a transition away from dominantly brittle, pressure-sensitive deformation mechanisms with increasing normal stress [20]. Smectite–quartz mixtures containing $\leq$50% quartz also exhibit a transition at normal stresses of 30–40 MPa, although the change in the slope of the failure envelope becomes less pronounced with increased quartz content. The failure envelope for illite shale and smectite–quartz mixtures containing $>$70% quartz exhibit brittle, pressure-sensitive failure over the entire range of normal stresses studied (Fig. 5).

3.2. Velocity dependence of sliding friction

As shown previously by Saffer et al. [20], Ca-smectite exhibits velocity-weakening behavior under a limited set of conditions of low normal stress and upstep sliding velocities $<$10 μm/s. Here, we augment and extend this data set to better resolve the transition from velocity weakening to velocity strengthening. We find that

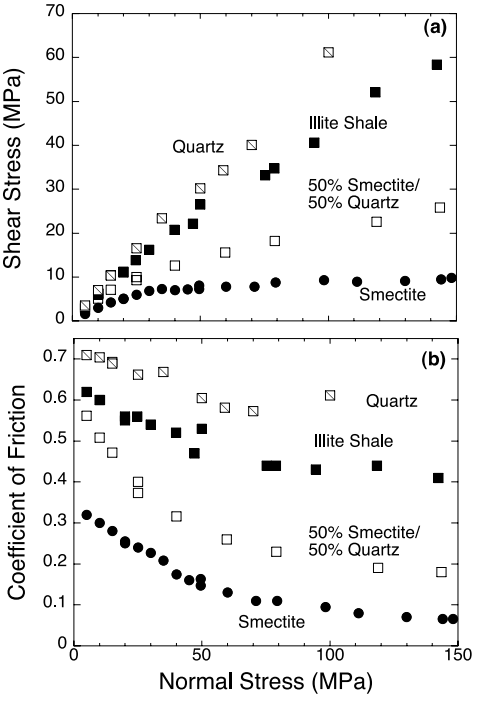

Fig. 5. (a) Experimentally determined failure envelopes (shear stress values during steady shear at 10 μm/s) for illite shale and smectite, at normal stresses up to 150 MPa. Data for 100% quartz (data from [32] and [43]) and 50% quartz–smectite mixtures are shown for comparison. (b) Coefficient of friction for the same materials, as a function of normal stress. Note the decrease in friction coefficient with increased normal stress for all materials. Experimental reproducibility of data plotted in (a) and (b) is shown by results of experiments under identical conditions, which overlay in most cases.

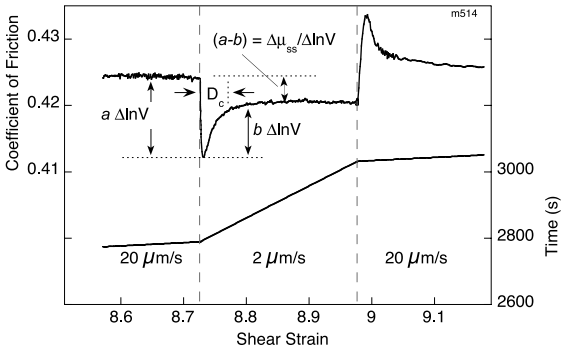

Fig. 6. Detailed view of a velocity step in illite shale. The initial change in friction coefficient scales as the friction parameter $a\times\ln(V/V_0)$ and is always of the same sign as the velocity change. The decay to a new steady-state value of sliding friction scales as the friction parameter $b\times\ln(V/V_0)$ and is of the opposite sign. Frictional velocity dependence is defined as $(a-b)=\Delta\mu/\Delta\ln V$, where V is sliding velocity.

smectite exhibits a clear transition to velocity weakening at sliding velocities <20 μm/s and normal stresses below 40 MPa (Figs. 7a and 8a,b). In our experiments, smectite exhibited velocity-strengthening behavior $[(a-b)>0]$ at sliding velocities >20 μm/s for the entire range of normal stresses studied (5–150 MPa), and for upstep velocities <20 μm/s at normal stresses above 40 MPa (Fig. 8). We observe a minimum value of $(a-b)=-0.003$ at a normal stress of 5 MPa and a sliding velocity of 10 μm/s. Maximum values of $(a-b)$ of 0.003–0.0053 observed at normal stresses >50 MPa and sliding velocities of 200 μm/s are consistent with the value of 0.005 reported by Morrow et al. [15] for similar normal stresses and sliding velocities under saturated conditions. We find that for a given normal stress and sliding velocity, the friction parameter $(a-b)$ does not vary over a range of shear strain from ~3 to 14 (Fig. 8c).

With increased quartz content, smectite–quartz mixtures exhibit a transition from complex velocity-dependent frictional behavior for pure smectite, to velocity-weakening frictional behavior typically observed for highly localized shear in quartz gouge (Fig. 7b). At a normal stress of 25 MPa, and for upstep sliding velocities of 100–200 μm/s, $(a-b)$ decreases systematically with quartz content, from values of 6×10^{-4} for 10% quartz to

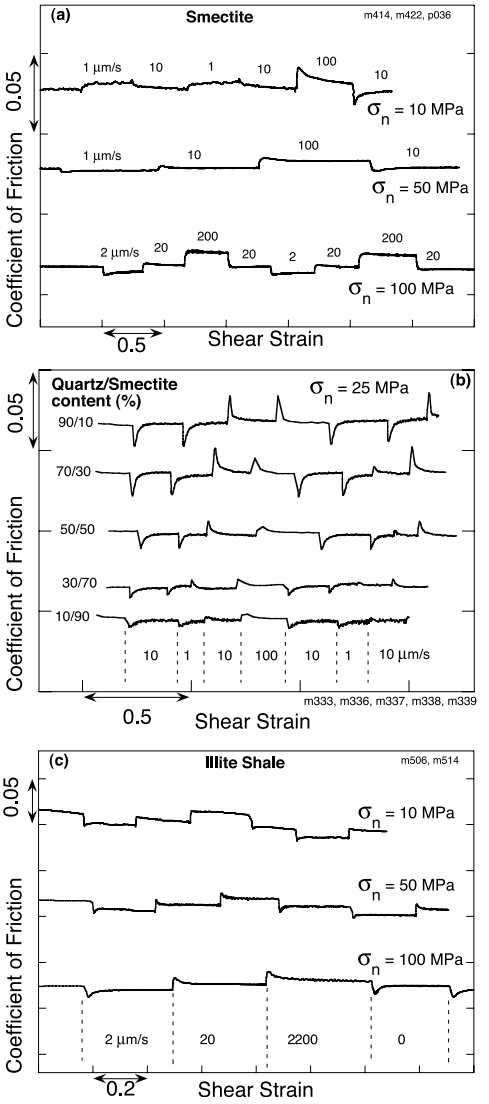

Fig. 7. Examples of velocity steps for (a) 100% Ca-smectite gouge (b) smectite–quartz mixtures, and (c) illite shale gouge. The smectite and illite shale data are shown at normal stresses of 10, 50, and 100 MPa, at shear strains of ~7–10. The smectite–quartz mixtures are shown at 25 MPa normal stress, for a range of quartz contents. Note that smectite exhibits velocity weakening at low normal stresses and velocity strengthening at high normal stresses, whereas illite shale exhibits only velocity strengthening. Friction curves are plotted at the same scale, but are offset on the y-axis for clarity (see Fig. 5 for absolute values of friction coefficient for each normal stress).

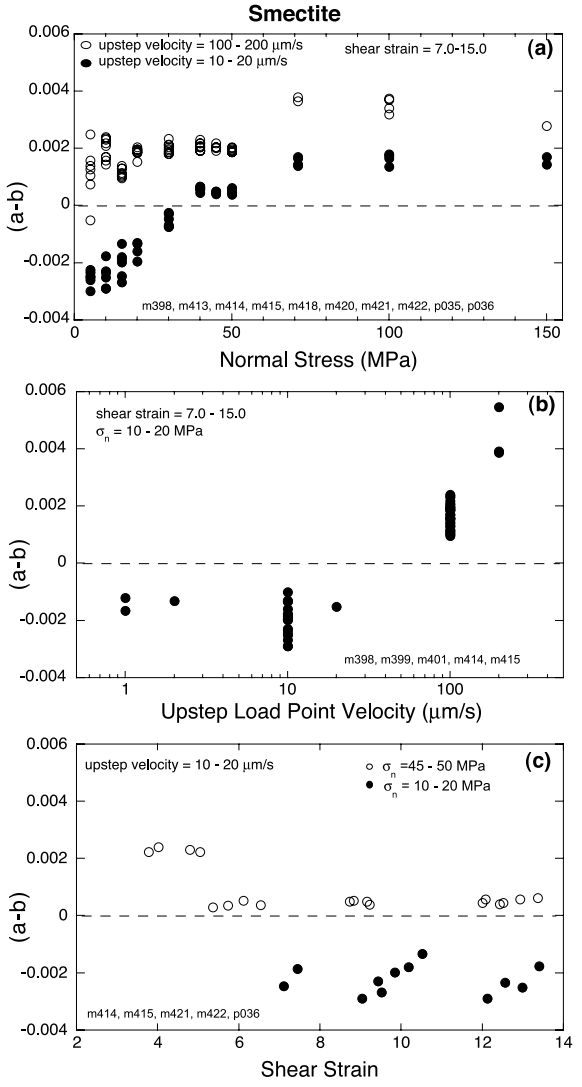

Fig. 8. Frictional velocity dependence for Ca-smectite gouge, as a function of (a) normal stress, (b) load point velocity, and (c) shear strain. The dependence of $(a-b)$ on normal stress is shown for shear strains of 7.0–15.0, and for upstep velocities of 10–20 μm/s (black circles) and 100–200 μm/s (open circles). The dependence of $(a-b)$ on sliding velocity is also shown for shear strains of 7.0–15.0, and for a normal stress of 10 MPa (panel b). The dependence on shear strain is shown for normal stresses of 10–20 MPa (black circles) and 45–50 MPa (open circles), and for upstep sliding velocities of 10–20 μm/s. Smectite exhibits a transition from velocity-weakening behavior at low normal stresses ($\sigma_n < 35$ MPa) and upstep sliding velocities < 20 μm/s, as shown in panels a and b, but $(a-b)$ does not vary with shear strain over the range studied (panel c). Experimental reproducibility is shown by results of multiple experiments under identical conditions.

-2×10^{-4} for 90% quartz (Figs. 7b and 9). For upstep sliding velocities of 10–20 μm/s, gouges containing $<50\%$ quartz generally exhibit velocity-weakening behavior, with values of $(a-b)$ ranging from -7×10^{-4} to 2×10^{-4} (Figs. 7b and 9). Values of $(a-b)$ become positive, increasing to 4×10^{-4} to 9×10^{-4}, for gouge containing 70% quartz, and then become negative again at quartz contents of 90%. For lower quartz contents ($<70\%$), gouges exhibit the complex velocity-dependent behavior of $(a-b)$ observed in pure smectite, whereas at high quartz contents ($>70\%$), $(a-b)$ exhibits little dependence on sliding velocity. For all mixtures, the absolute value of $(a-b)$ is less than 0.002.

In contrast, illite shale exhibits only velocity-strengthening behavior over the entire range of normal stresses (5–150 MPa) and sliding velocities (0.1–200 μm/s) (Figs. 7c and 10). Values of $(a-b)$ range from $\sim$0.0015 to 0.004, and unlike smectite, do not vary appreciably with normal stress (Fig. 10a) or velocity (Fig. 10b). For illite gouge, values of $(a-b)$ are also generally independent of shear strain at normal stresses of 10–50 MPa (Fig. 10c).

3.3. Constitutive modeling

We modeled data from velocity-step tests using the rate and state variable friction constitutive law:

$$\mu = \mu_0 + a\ln\left(\frac{V}{V_0}\right) + b\ln\left(\frac{V_0\theta}{D_c}\right) \quad (1)$$

$$\frac{d\theta}{dt} = \left(1-\frac{V\theta}{D_c}\right), \text{ Dieterich Law} \quad (2)$$

where μ_0 is a reference friction value, θ is a state variable, and the other terms have been defined above. We focus here only on the Dieterich Law (see [9] for a discussion of other rate and state friction laws), for which the friction state variable has been connected to the average lifetime of contact junctions for extended solid surfaces [29] and to the porosity or packing state of sheared granular gouge layers [30]. To model laboratory data and account for finite stiffness of the testing apparatus, Eqs. 1 and 2 are coupled with a descrip-

tion of elastic interaction between the gouge layers and experimental apparatus:

$$\frac{d\mu}{dt} = k(V_{lp} - V) \quad (3)$$

where k is the apparatus stiffness normalized by normal stress (for our 10 cm × 10 cm surfaces, k is 1×10^{-3}/μm for a normal stress of 25 MPa) and V_{lp} is load point velocity.

We used fifth-order Runge-Kutta numerical intergration with adaptive step-size control to solve Eqs. 2 and 3 simultaneously, using Eq. 1 as a constraint. To determine best-fit values for the constitutive parameters a, b, and D_c we use an iterative, least-squares method to solve the nonlinear inverse problem. We solve the linearized inverse problem by singular-value decomposition of the matrix of partial derivatives, using a method similar to that of Reinen and Weeks [31], except that we use variable damping to reduce convergence time. The unweighted chi square error for a typical model fit (Fig. 11a) is ≤0.0003 and the variance, given by the chi square error normalized by the data set degrees of freedom (there are four model parameters to be fit and a

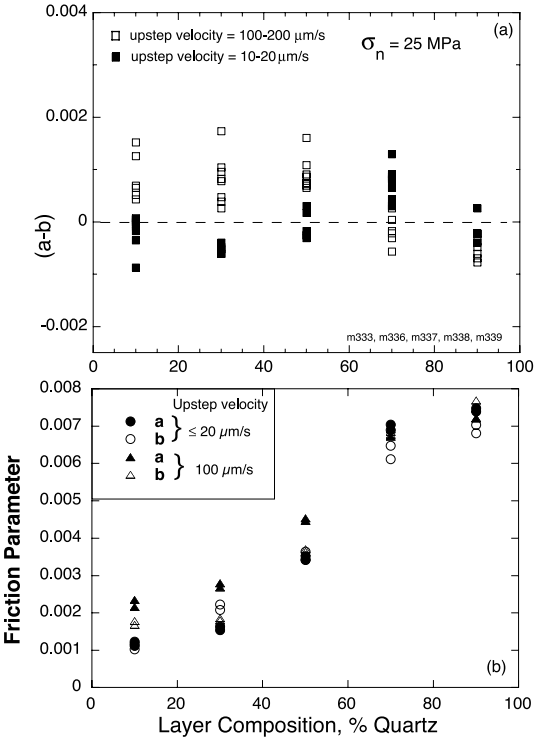

Fig. 9. (a) Frictional velocity dependence and (b) friction parameters a and b for smectite–quartz mixtures at 25 MPa normal stress, as a function of quartz content. Data are shown for upstep sliding velocities of 10–20 μm/s and 100–200 μm/s.

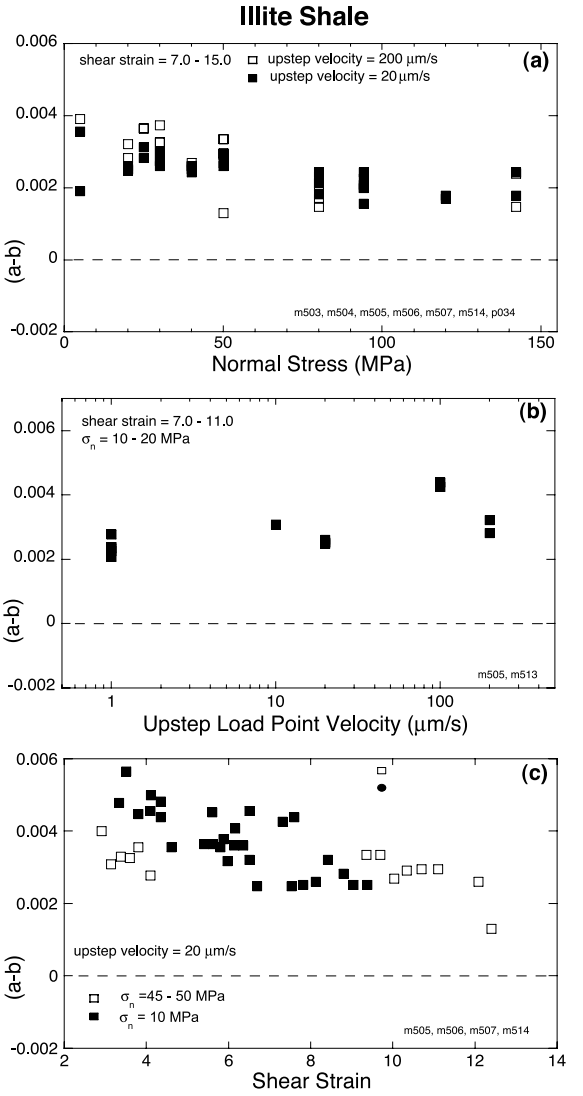

Fig. 10. Frictional velocity dependence for illite shale gouge, as a function of (a) normal stress, (b) load point velocity, and (c) shear strain, plotted for the same range of conditions as results for Ca-smectite (Fig. 8). Unlike smectite, illite shale exhibits only velocity-strengthening behavior, and values of $(a-b)$ do not vary significantly with normal stress, sliding velocity, or shear strain.

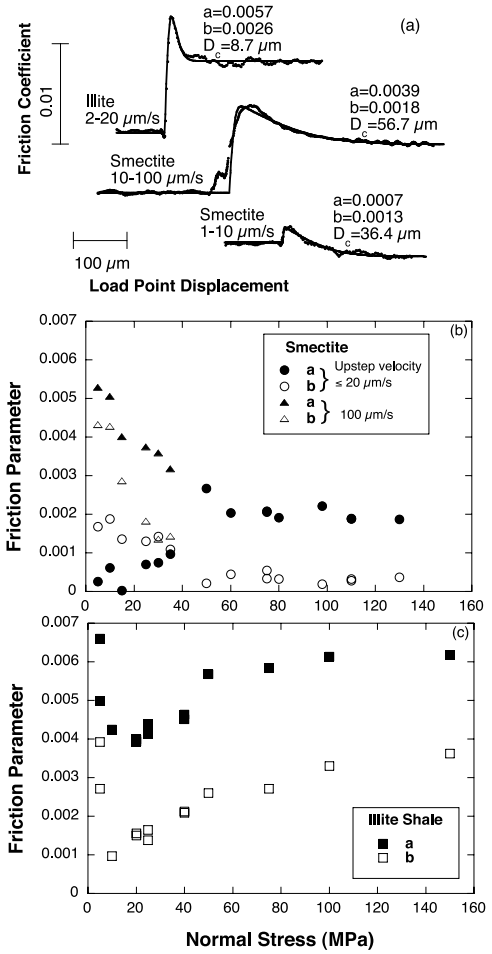

Fig. 11. (a) Modeling results for constitutive parameters (a, b, and D_c) (solid curves) and friction data (black circles) for velocity steps in illite shale (top) and smectite (middle and bottom) gouges. (b,c) Modeled friction parameters a (black symbols) and b (open symbols) for smectite (panel b) and illite shale (panel c) as a function of normal stress. For smectite (panel b), data are divided into values for upstep velocities ≤ 20 μm/s (circles) and 100 μm/s (triangles).

typical velocity step consists of 500 to 1000 data points), is typically $\leq 5\times10^{-7}$. Formal error estimates are calculated from the covariance matrix and are reported here as one standard deviation (Table 2). These formal errors are smaller than uncertainties associated with experimental reproducibility, which we evaluated by conducting and modeling multiple velocity steps in each experiment and by repeating experiments under identical conditions. Experimental uncertainties are typically 2–3 times the formal standard deviations (Table 2). Velocity increases and decreases show similar behavior (Fig. 7) but we report detailed modeling on only velocity increases.

The Dieterich rate and state friction law provides good fits to our experimental data. In each case, the visual comparisons of data and model are very close, allowing for some misfit associated with data noise (Fig. 11a). The rate/state friction behavior of smectite gouge is complex, reflecting its variation with normal stress and slip velocity (Figs. 7 and 8). For upstep velocities below 20 μm/s, both of the friction parameters a and b undergo a transition at a normal stress of 40 MPa (Fig. 11b). With increasing normal stress, the parameter a increases and b decreases at about 40 MPa. For higher upstep velocities, smectite gouge exhibits higher values of a and b compared to the values for velocities <20 μm/s and normal stress below 40 MPa (Fig. 11b). The friction parameter b is very low for normal stresses above 40 MPa, and both friction parameters are independent of slip rate for normal stresses above 40 MPa. For normal stresses below 40 MPa, the critical slip distance is higher for higher velocity (Table 2) and for velocities ≤ 20 μm/s D_c increases with normal stress. Note however that when the parameter b is near zero D_c is unconstrained, which is consistent with the large error estimates at the highest normal stresses (Table 2).

For smectite–quartz mixtures, values of both a and b increase systematically with increased quartz content (Fig. 9b; Table 2). For low quartz content ($<70\%$), the values of both a and b are slightly larger at higher upstep sliding velocities. Despite the large change observed in both a and b over the range of gouge compositions (Fig. 9b), the velocity dependence ($a-b$) varies over a small range (between -2×10^{-4} and 2×10^{-4}). For the mixtures with low quartz content, ($a-b$) is negative at lower velocity and the gouge exhibits a transition to velocity-strengthening behavior at upstep velocities above 100 μm/s, consistent with the behavior we observe for pure smectite. D_c increases systematically with decreasing quartz content (Table 2).

For illite shale gouge, we find that the friction parameter a exceeds the evolution parameter b throughout the range of velocities and normal stresses studied (Fig. 11c), consistent with the results showing steady-state velocity strengthening (Fig. 8). Both friction parameters for illite show a minimum at normal stresses of 10–20 MPa and maximum values at 5 MPa. The critical slip distance, D_c, is 10–30 μm for illite shale, independent of normal stress.

3.4. Dilatancy

Gouge layer volume changes associated with changes in sliding velocity are important for understanding strength and fabric development (e.g., [32]), as well as for rupture models that couple constitutive friction laws and pore fluid pressure (e.g., [28]). We report a measure of gouge layer dilatancy, $\alpha = \Delta h/\Delta \log V$, where h is gouge layer thickness and V is sliding velocity (e.g.,

Table 2
Constitutive parameters for least-squares fit of the Dieterich Law

σ_n (MPa)	a	a S.D.	b	b S.D.	$a-b$	D_c, (μm)	D_c S.D.	V_f (μm/s)	Gouge
5	0.0003	0.00038	0.0017	0.00037	−0.0014	12.6	4.68	10	Smectite
5	0.0053	0.00008	0.0043	0.00008	0.0010	124.5	5.63	100	Smectite
10	0.0006	0.00020	0.0019	0.00019	−0.0013	15.6	2.38	10	Smectite
10	0.0051	0.00007	0.0043	0.00008	0.0008	137.9	5.70	100	Smectite
15	0.0000	0.00014	0.0014	0.00013	−0.0013	20.6	3.19	10	Smectite
15	0.0040	0.00007	0.0029	0.00006	0.0011	68.7	2.53	100	Smectite
25	0.0007	0.00008	0.0013	0.00007	−0.0006	36.4	3.60	10	Smectite
25	0.0037	0.00006	0.0018	0.00005	0.0019	56.7	2.60	100	Smectite
30	0.0008	0.00005	0.0014	0.00005	−0.0007	41.4	2.16	10	Smectite
30	0.0036	0.00005	0.0014	0.00005	0.0022	48.1	2.56	100	Smectite
35	0.0010	0.00008	0.0011	0.00007	−0.0001	29.4	2.84	10	Smectite
35	0.0032	0.00004	0.0014	0.00003	0.0018	62.0	2.29	100	Smectite
50	0.0027	0.00003	0.0002	0.00004	0.0025	69.6	37.74	20	Smectite
60	0.0020	0.00002	0.0004	0.00002	0.0016	61.1	5.79	20	Smectite
75	0.0021	0.00001	0.0003	0.00001	0.0017	83.3	5.84	20	Smectite
80	0.0019	0.00002	0.0003	0.00004	0.0016	113.4	33.55	20	Smectite
98	0.0022	0.00002	0.0002	0.00009	0.0020	131.3	140.61	20	Smectite
130	0.0019	0.00001	0.0004	0.00011	0.0015	1541.9	531.95	20	Smectite
25	0.0011	0.00005	0.0012	0.00004	0	41.5	2.33	10	10% Quartz
25	0.0024	0.0001	0.0018	0.00009	0.0006	50.2	4.93	100	10% Quartz
25	0.0015	0.00003	0.0022	0.00003	−0.0007	20.1	0.38	10	30% Quartz
25	0.0028	0.00007	0.0018	0.00007	0.001	25.9	1.34	100	30% Quartz
25	0.0034	0.00005	0.0034	0.00005	0	25.8	0.51	10	50% Quartz
25	0.0045	0.00009	0.0037	0.00009	0.0008	28.7	1.01	100	50% Quartz
25	0.0070	0.00013	0.0061	0.00012	0.0009	20.9	0.56	10	70% Quartz
25	0.0067	0.00021	0.0069	0.00021	−0.0001	19.1	0.84	100	70% Quartz
25	0.0075	0.00013	0.0068	0.00013	0.0007	11.9	0.29	10	90% Quartz
25	0.0072	0.00034	0.0072	0.00033	0	12.2	0.72	100	90% Quartz
5	0.0066	0.00015	0.0039	0.00014	0.0027	36.4	2.01	20	Illite shale
10	0.0042	0.00015	0.0010	0.00014	0.0033	10.0	2.09	20	Illite shale
20	0.0039	0.00008	0.0015	0.00008	0.0024	23.9	1.73	20	Illite shale
25	0.0041	0.00008	0.0014	0.00008	0.0028	14.3	1.11	20	Illite shale
40	0.0046	0.00009	0.0021	0.00009	0.0025	21.8	1.19	20	Illite shale
50	0.0057	0.00012	0.0026	0.00012	0.0031	8.7	0.49	20	Illite shale
75	0.0058	0.00008	0.0027	0.00007	0.0031	17.3	0.65	20	Illite shale
100	0.0061	0.00005	0.0033	0.00005	0.0028	20.4	0.43	20	Illite shale
150	0.0062	0.00007	0.0036	0.00006	0.0026	25.2	0.57	20	Illite shale

All velocity steps were a factor of 10. V_f is the final (upstep) velocity. See Fig. 11.

[33]). To calculate α, we de-trend measured layer thickness to account for monotonic thinning due to simple shear (e.g., [34]).

For both smectite and illite shale, α is positive (indicating dilation with increased sliding velocity) under all experimental conditions we explored, except in the case of smectite at normal stresses <40 MPa and upstep sliding velocities <20 μm/s. For smectite, α ranges from -0.2 to 2.5 μm; values for illite shale range from 0.65 to 3.2 μm. For both smectite and illite shale, values of α are scattered but exhibit no systematic variation over the range of normal stresses investigated.

4. Discussion

4.1. Frictional strength

We suggest that the observed peak and subsequent decrease in frictional strength with strain, for shear strains of 1–5, reflects shear-enhanced compaction and alignment of platy clay minerals during early stages of shearing (Fig. 4). This stress–strain response is commonly observed in clays and clay-rich soils, and is generally interpreted to result from alignment of clay particles (e.g., [18,21,35]). The development of preferred grain orientations in smectite along the edges of shears observed by Saffer et al. [20] is consistent with this interpretation. The observation of a less pronounced peak stress in illite shale than in pure smectite is also consistent with observations from smectite–quartz mixtures, which exhibit a less pronounced peak stress with decreasing clay content [36]. This further supports the hypothesis that clay grain alignment is a key factor controlling the strength and frictional behavior of clay-rich gouges.

The transition to pressure-insensitive deformation in pure smectite, observed at 30–40 MPa normal stress, occurs at a significantly lower normal stress than for other materials (quartz, carbonate, or granite, for example). Saffer et al. [20] (following Bird's [22] interpretation), suggested that this transition is controlled by the existence of a weak hydrated glide plane within the clay mineral structure at low normal stress, but did not rule out the possibility that stress-induced dehydration occurred during the experiment, expelling interlayer water into the intergranular pore space and resulting in undetected high pore pressures. Alternatively, the kink in the failure envelope of smectite-rich gouge may reflect a change from increasing contact area between grains with increased stress below 40 MPa, to complete contact area between aligned platy clay grains at greater normal stresses. The absence of a similar transition to pressure-independent deformation in high quartz content mixtures and illite shale, which does not contain hydrous clays but does contain quartz and feldspar grains, is consistent with both explanations.

Our experimentally determined sliding friction coefficients for smectite ($\mu = 0.07$–0.30) are comparable to values of ~ 0.13–0.40 reported by Morrow et al. [14–16] for pure smectite under both vacuum-dried ($\mu = \sim 0.3$–0.4) and saturated ($\mu = 0.13$–0.3) conditions in triaxial experiments at room temperature and normal stresses of 1–400 MPa. Friction coefficients for smectite–quartz mixtures ($\mu = \sim 0.2$–0.53) and the observed systematic increase with increased quartz content are also consistent with previous work [18,19]. Friction coefficients for illite shale ($\mu = 0.41$–0.63) in our experiments are comparable to values of ~ 0.4 reported by Morrow et al. [14,15] for similar materials under both wet and dry conditions and a value of 0.49 reported by Moore et al. [17] for a temperature of 200°C and at normal stresses up to 400 MPa, under both saturated and dry conditions. Moore et al. [17] observed slight strengthening of illite gouge at temperatures of 400°C and 600°C, although this may be an artifact of the sample geometry used, and is probably not relevant to gouge behavior at depths near the onset of seismogenic behavior, which occurs at projected temperatures of ~ 150°C.

Our experimental results for illite shale, which contains $\sim 60\%$ illite and 23% quartz, indicate that it is significantly stronger than both pure Ca-smectite and 50% quartz–smectite mixtures (Figs. 4 and 5). Our experimentally determined failure envelopes are consistent with previous work on similar materials, including synthetic quartz–clay mixtures (e.g., [19,36]). This result

suggests that in mixed-mineralogy gouges with appreciable clay content, the change from smectite to illite may result in an increase in frictional strength (e.g., [26]).

4.2. Velocity dependence of sliding friction

If smectite transformation to illite controls the onset of unstable slip, velocity-weakening frictional behavior of illite gouge is a necessary condition. However, illite shale exhibited only velocity-strengthening behavior over the range of experimental conditions we explored. The values of $(a-b)$ (0.0015–0.004) reported here are consistent with a value of $(a-b)=0.005$ reported by Morrow et al. [15] for both dry and saturated illite shale under normal stresses of 100 and 300 MPa. Although we cannot rule out the possibility of velocity-weakening behavior at higher temperatures or larger shear strains, our results are inconsistent with the hypothesis that transformation of stably sliding smectite to illite controls the updip limit of the seismogenic zone.

For pure smectite, the friction parameter b decreases with increasing normal stress, reaching a constant value near zero above normal stresses of $\sim$40 MPa (Fig. 11b). As noted by Scholz [37], the parameter b measures the evolution of contact area with time. We suggest that at normal stresses $> \sim$40 MPa, the clay gouge particles are in complete contact, causing both the observed transition to pressure-independent strength, and a decrease of b to near zero. One implication of near zero values of b is that the real area of frictional contact does not change after a velocity step. As such, D_c is unconstrained (cf., Table 2) because it is a measure of the displacement associated with changes in contact area. Importantly, in mixed-mineralogy gouges containing quartz and/or plagioclase, parameter b does not decrease to near zero with increased normal stress, and we do not observe a transition to pressure-independent shear strength. This suggests that with increased non-clay mineral content, the contact area and its change with time are less affected by increased normal stress. Further work, including microstructural observations of sheared gouge layers, is clearly needed.

For pure smectite, the friction parameter a depends on both sliding velocity and normal stress. At sliding velocities >100 μm/s the parameter a decreases with normal stress (Fig. 9b), whereas for sliding velocities ≤ 20 μm/s a increases with normal stress. We attribute this behavior to increased fabric disruption at higher sliding velocities and also at lower normal stresses, both resulting in larger values of the direct effect. This interpretation is supported by the observation that increased quartz content leads to larger values of a (a larger direct effect) (Fig. 9b).

4.3. Dilatancy and potential pore pressure effects

Although we did not explore the role of saturation within gouge layers, direct measurements of dilatancy or compaction provide some insight into the potential physical effects of fluids in saturated gouge. We note that α is positive for illite shale in all of our experiments (and for smectite under most experimental conditions we explored) – indicating dilatancy with increased sliding velocity. This volume increase should result in dilatancy hardening and thus further velocity strengthening in saturated gouges, by decreasing pore pressure during slip (dilation), rather than potentially causing weakening by transient pore pressure increase (e.g., [28]).

5. Alternative hypotheses for the updip limit of seismogenesis

Although our results are not comprehensive over all potential experimental conditions (i.e., saturation, temperature), they suggest that other thermally or depth-dependent processes may be more important in controlling the onset of frictional velocity weakening (and unstable slip) than clay transformation (e.g., [7]) (a subset of these processes is shown in Fig. 12). These processes include but are not limited to (1) shear localization and increased shear strain (Fig. 12b) (e.g., [9,32]), (2) porosity reduction and increased consolidation state of gouge (Fig. 12c) (e.g., [8,38]), (3) increasing effective stress due to increased total

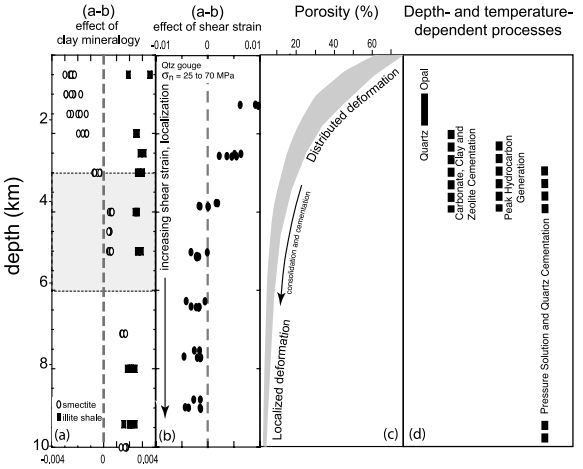

Fig. 12. Summary of depth-dependent changes in frictional behavior and proposed mechanisms for the updip limit of seismicity in subduction thrusts. (a) Frictional velocity dependence for smectite (open circles) and illite shale (black squares), for upstep velocities of 20 μm/s, plotted with increasing depth on the basis of our experimental results, assuming that effective stress increases by 10 MPa/km. Grey shaded region shows depth range for smectite transformation (after [47,48]). Dashed line denotes velocity-neutral behavior. Note that both materials exhibit only velocity-strengthening behavior at normal stresses above those corresponding to ~4 km depth, and illite shale is velocity strengthening at all depths. (b) Frictional velocity dependence of sheared quartz gouge, plotted as a function of depth assuming a linear relation between depth and shear strain (data from [32]). With increased shear strain and localization, quartz exhibits a shift from velocity-strengthening to velocity-weakening behavior (e.g., [9]). (c) Porosity loss and associated transition from distributed deformation to localized slip hypothesized to explain the updip limit of seismicity in accretionary wedges (e.g., [38]). (d) A suite of diagenetic and dehydration processes, including quartz phase transformation, cementation, fluid release from hydrous clays and hydrocarbon generation, and pressure solution, all beginning at ~1–4 km depth (after [7]).

overburden and possibly variations in pore pressure (e.g., [7,10]), and (4) pressure solution, silica or carbonate cementation, fluid release from low-T dehydration and hydrocarbon generation processes, and other low-temperature diagenetic alteration leading to increased gouge consolidation (Fig. 12d) (e.g., [7]).

Detailed experimental and theoretical studies have demonstrated that increased shear strain is linked to slip localization and velocity-weakening behavior (Fig. 12b), whereas distributed deformation is linked to velocity-strengthening behavior (e.g., [9,32,39–40]). The transition from pervasive to localized slip in granular materials, sediments, and sedimentary rocks depends upon both confining pressure and porosity (e.g., [41]). At lower initial porosity (a result of compaction), the tendency for localized deformation is increased. As suggested by Marone and Scholz [8] and Davis et al. [38], the onset of seismicity at depths of 3–5 km may reflect a transition from unconsolidated, gouge-rich fault zones characterized by distributed deformation to highly consolidated fault zones (Fig. 12c). In this model, consolidated gouge behaves as a solid rather than a particulate (granular) material, and thus the upper frictional stability transition represents a critical consolidation state, dependent on temperature, fault loading rate, and mineralogy. This hypothesis is supported by the observation that changes in frictional behavior are associated with compaction of simulated granular gouges [42,43]. In addition to its effects on compaction state that may cause a transition to localized deformation and velocity-weakening behavior, increasing effective stress with depth also drives velocity-weakening materials toward unstable slip by increasing the magnitude of the stability parameter ζ as discussed above [10].

Diagenetic processes (such as cementation) and pressure solution influence porosity, deformation style, rigidity, and may affect seismic coupling (e.g., [44]). In this sense, these processes are closely linked to the transformation from distributed deformation to localized shear with increasing depth and temperature (Fig. 12d). It is important to note that smectite transformation may be accompanied by silica cementation as SiO_2 is produced (e.g., [45,46]). This could serve to alter the mineralogical composition of marine sediments and fault gouge with the progressive smectite transformation to illite. These effects, as well as mineralogical changes associated with other diagenetic processes – such as zeolite cementation or opal-CT to quartz transformation – are not captured in our experiments. Understanding the associated changes in frictional behavior would require testing of natural gouges or shales that have

undergone various stages of clay transformation. Vein filling by framework silicates and carbonates may also affect frictional properties along the plate interface, as well as affecting a shift from distributed to localized slip. Thus, a wide range of mechanical and chemical processes that are active at temperatures of ~60–150°C and depths of ~2–4 km may partially control the updip limit of the seismogenic zone (e.g., [7]).

6. Conclusions

Our experimental results indicate that the transformation of smectite to illite within fault gouge, and within marine sediments from which gouge along subduction thrusts is derived, should cause an increase in frictional strength; however we do not observe a transition from velocity-strengthening to velocity-weakening frictional behavior as hypothesized by others. Smectite exhibits velocity-strengthening frictional behavior over much of the range of experimental conditions, but exhibits velocity-weakening behavior at low normal stresses and low sliding velocities. Illite shale exhibits only velocity-strengthening behavior over the entire range of normal stresses, shear strains, and sliding velocities explored in our study. These results are inconsistent with the hypothesis that transformation from smectite to illite causes a transition from stable sliding to stick-slip behavior along subduction megathrusts. Additional experiments are clearly needed to more comprehensively evaluate this hypothesis, by systematically evaluating the effects of increased temperature, saturation, mineralogical changes, and diagenesis on constitutive properties of clay-rich gouges.

On the basis of our experimental results, we suggest that mechanisms other than clay transformation may be important in controlling the updip limit of seismogenic faulting. These include: consolidation state of gouge and sediments, a transition from distributed to localized shear (e.g., [8,39]), quartz cementation and pressure solution that may be associated with clay transformation (e.g., [7]), and increasing effective stress related to progressive burial, probably mediated by pore pressure variations (e.g., [7]).

Acknowledgements

This work was supported by National Science Foundation (NSF) grants EAR-02-29585 to D.M.S. and OCE-01-96462 to C.M. We thank Mike Underwood for help with XRD analyses and Kevin Frye for help with running experiments. We also thank Sue Bilek, Kelin Wang, and Stefano Mazzoni for their constructive reviews. *[SK]*

References

[1] R.D. Hyndman, M. Yamano, D.A. Oleskevich, The seismogenic zone of subduction thrust faults, The Island Arc 6 (1997) 244–260.
[2] T. Shimamoto et al., A simple rheological framework for comparative subductology, in: K. Akai, R. Dmowska (Eds.), Relating Geophysical Structures and Process: The Jeffreys Volume: Geophys. Monogr. Ser. 76, Am. Geophys. Union, Washington, DC, 1993, pp. 39–52.
[3] B.W. Tichelaar, L.J. Ruff, Depth of seismic coupling along subduction zones, J. Geophys. Res. 98 (1993) 2017–2037.
[4] R.H. Sibson, Fault zone models, heat flow, and the depth distribution of earthquakes in the continental crust of the United States, Bull. Seis. Soc. Am. 72 (1982) 151–163.
[5] C.H. Scholz, The Mechanics of Earthquakes and Faulting, Cambridge Press, New York, 1990, 439 pp.
[6] S.M. Peacock, R.D. Hyndman, Hydrous minerals in the mantle wedge and the maximum depth of subduction thrust earthquakes, Geophys. Res. Lett. 16 (1999) 2517–2520.
[7] J.C. Moore, D.M. Saffer, Updip limit of the seismogenic zone beneath the accretionary prism of southwest Japan: An effect of diagenetic to low-grade metamorphic processes and increasing effective stress, Geology 29 (2001) 183–186.
[8] C. Marone, C. Scholz, The depth of seismic faulting and the upper transition from stable to unstable slip regimes, Geophys. Res. Lett. 15 (1988) 621–624.
[9] C. Marone, Laboratory-derived friction laws and their application to seismic faulting, Annu. Rev. Earth Planet. Sci. 26 (1998) 643–696.
[10] C.H. Scholz, Earthquakes and friction laws, Nature 391 (1998) 37–42.
[11] A.M. Pytte, R.C. Reynolds, The thermal transformation of smectite to illite, in: T.H. McCulloh, N.D. Naeser (Eds.), Thermal Histories of Sedimentary Basins, Springer, New York, 1988, pp. 133–140.
[12] D.A. Oleskevich, R.D. Hyndman, K. Wang, The updip and downdip limits to great subduction earthquakes: Thermal and structural models of Cascadia, South Alas-

ka, SW Japan, and Chile, J. Geophys. Res. 104 (1999) 14965–14991.
[13] P. Vrolijk, B.A. VanderPluijm, Clay Gouge, J. Struct. Geol. 21 (1999) 1039–1048.
[14] C.A. Morrow, L.Q. Shi, J.D. Byerlee, Strain hardening and strength of clay-rich fault gouges, J. Geophys. Res. 87 (1982) 6771–6780.
[15] C. Morrow, B. Radney, J.D. Byerlee, Frictional strength and the effective pressure law of montmorillonite and illite clays, in: B. Evans (Ed.), Fault Mechanics and Transport Properties of Rocks; A Festschrift in Honor of W.F. Brace, Academic Press, San Diego, CA, 1992, pp. 69–88.
[16] C.A. Morrow, D.E. Moore, D.A. Lockner, The effect of mineral bond strength and absorbed water on fault gouge frictional strength, Geophys. Res. Lett. 27 (2000) 815–818.
[17] D.E. Moore, R. Summers, J.D. Byerlee, Sliding behavior and deformation textures of heated illite gouge, J. Struct. Geol. 11 (1989) 329–342.
[18] J.F. Lupini, A.E. Skinner, P.R. Vaughan, The drained residual strength of cohesive soils, Geotechnique 31 (1981) 181–213.
[19] J.M. Logan, K.A. Rauenzahn, Frictional dependence of gouge mixtures of quartz and montmorillonite on velocity, composition, and fabric, Tectonophysics 144 (1987) 87–108.
[20] D.M. Saffer, K.F. Frye, C. Marone, K. Mair, Laboratory results indicating complex and potentially unstable frictional behavior of smectite clay, Geophys. Res. Lett. 28 (2001) 2297–2300.
[21] J.K. Mitchell, Fundamentals of Soil Behavior, 2nd edn., Wiley, New York, 1993, 437 pp.
[22] P. Bird, Hydration-phase diagrams and friction of montmorillonite under laboratory and geologic conditions, with implications for shale compaction, slope stability, and strength of fault gouge, Tectonophysics 107 (1984) 235–260.
[23] G.F. Moore et al., New insights into deformation and fluid flow processes in the Nankai Trough accretionary prism: Results of Ocean Drilling Program Leg 190, Geochem. Geophys. Geosyst. (2001) Paper number 2001GC000166.
[24] M.B. Underwood et al., Sediment geochemistry, clay mineralogy, and diagenesis: A synthesis of data from leg 131, Nankai Trough, Proc. ODP Sci. Results 131 (1993) 343–363.
[25] M.B. Underwood, D.M. Saffer, J. Steurer et al., Along-strike variations in clay mineralogy and diagenesis: implications for up-dip limit of the Nankai seismogenic zone, EOS Trans. Am. Geophys. Union 81 (2000) F-1248.
[26] P. Vrolijk, On the mechanical role of smectite in subduction zones, Geology 18 (1990) 703–707.
[27] X. Deng, M.B. Underwood, Abundance of smectite and the location of a plate-boundary fault, Barbados accretionary prism, Geol. Soc. Am. Bull. 113 (2001) 495–507.
[28] P. Segall, J.R. Rice, Dilatancy, compaction, and slip instability of a fluid infiltrated fault, J. Geophys. Res. 100 (1995) 22155–22173.
[29] J.H. Dieterich, B. Kilgore, Direct observation of frictional contacts: new insights for state-dependent properties, Pure Appl. Geophys. 143 (1994) 283–302.
[30] C. Marone, B. Raleigh, C.H. Scholz, Frictional behavior and constitutive modeling of simulated fault gouge, J. Geophys. Res. 95 (1990) 7007–7025.
[31] L.A. Reinen, J.D. Weeks, Determination of rock friction constitutive parameters using an iterative least-squares inversion method, J. Geophys. Res. 98 (1993) 15937–15950.
[32] K. Mair, C. Marone, Friction of simulated fault gouge for a wide variety of velocities and normal stresses, J. Geophys. Res. 104 (1999) 28899–28914.
[33] C. Marone, B. Kilgore, Scaling of the critical slip distance for seismic faulting with shear strain in fault zones, Nature 362 (1993) 618–621.
[34] D. Scott, C. Marone, C. Sammis, The apparent friction of granular fault gouge in sheared layers, J. Geophys. Res. 99 (1994) 7231–7247.
[35] F.M. Chester, J.M. Logan, Composite planar fabric of fault gouge from the Punchbowl Fault, California, J. Struct. Geol. 9 (1987) 621–634.
[36] C. Marone, D.M. Saffer, K. Frye, Weak and potentially unstable frictional behavior of smectite clay, EOS Trans. Am. Geophys. Union 80 (1999) 689.
[37] C.H. Scholz, The Mechanics of Earthquakes and Faulting, 2nd edn., Cambridge University Press, New York, 2000, 464 pp.
[38] D.M. Davis et al., Porosity loss in the evolution of accretionary wedges; some mechanical and seismic implications, Proceedings of Workshop LXIII, USGS Red-Book Conference on the Mechanical Involvement of Fluids in Faulting, Open File Report–U.S. Geological Survey, OF 94-0228, 1994, 460–465.
[39] C. Marone, B.E. Hobbs, A. Ord, Coulomb constitutive laws for friction: contrasts in frictional behavior for distributed and localized shear, Pure Appl. Geophys. 139 (1992) 195–214.
[40] J.M. Logan, C.A. Dengo, N.G. Higgs, Z.Z. Wang, Fabrics of experimental fault zones: their development and relationship to mechanical behavior, in: B. Evans, T.F. Wong (Eds.), Fault Mechanics and Transport Properties of Rocks, Academic Press, 1992, pp. 33–67.
[41] J.-x. Zhang, D. Davis, T.-F. Wong, The brittle-ductile transition in porous sedimentary rocks; geological implications for accretionary wedge aseismicity, J. Struct. Geol. 15 (1993) 819–830.
[42] M. Nakatani, A new mechanism of slip weakening and strength recovery of friction associated with the mechanical consolidation of gouge, J. Geophys. Res. 103 (1998) 27239–27256.
[43] E. Richardson, C. Marone, Effects of normal stress vibrations on frictional healing, J. Geophys. Res. 104 (1999) 28857–28878.

[44] T. Byrne, Seismicity, slate belts and coupling along convergent plate boundaries, EOS Trans. Am. Geophys. Union 79 (1998) W-114.
[45] V.A. Colten-Bradley, Role of pressure in smectite dehydration: effects on geopressures and smectite to illite transformation, Am. Assoc. Pet. Geol. Bull. 71 (1987) 1414–1427.
[46] W.C. Elliot, G. Matisoff, Evaluation of kinetic models for the smectite to illite transformation, Clays Clay Min. 44 (1991) 77–87.
[47] D.M. Saffer, B.A. Bekins, Episodic fluid flow in the Nankai accretionary complex: Timescale, geochemistry, flow rates, and fluid budget, J. Geophys. Res. 103 (1998) 30351–30371.
[48] B.A. Bekins, A.M. McCaffrey, S.J. Dreiss, Influence of kinetics on the smectite to illite transition in the Barbados accretionary prism, J. Geophys. Res. 99 (1994) 18147–18158.